NANOROBOTS

Toward three-dimensional DNA industrial nanorobots

Feng Zhou[1,2,3,4]*, Heng Ni[3], Guolong Zhu[3,5], Lev Bershadsky[3], Ruojie Sha[4]*, Nadrian C. Seeman[4], Paul M. Chaikin[3]*

Nanoscale industrial robots have potential as manufacturing platforms and are capable of automatically performing repetitive tasks to handle and produce nanomaterials with consistent precision and accuracy. We demonstrate a DNA industrial nanorobot that fabricates a three-dimensional (3D), optically active chiral structure from optically inactive parts. By making use of externally controlled temperature and ultraviolet (UV) light, our programmable robot, ~100 nanometers in size, grabs different parts, positions and aligns them so that they can be welded, releases the construct, and returns to its original configuration ready for its next operation. Our robot can also self-replicate its 3D structure and functions, surpassing single-step templating (restricted to two dimensions) by using folding to access the third dimension and more degrees of freedom. Our introduction of multiple-axis precise folding and positioning as a tool/technology for nanomanufacturing will open the door to more complex and useful nano- and microdevices.

INTRODUCTION

Industrial robots, essential to modern manufacturing, take prefabricated parts, align them for further assembly, attach them, deposit them, and prepare for their next task. Fabrication of multicomponent systems both in living systems and in industry is done either by self-assembly or by active positioning and fixing/welding the separate parts. Catalysts and enzymes can capture and position two or more components for binding. They are natural industrial robots on the nanoscale (*1*, *2*). By convention, industrial robots are automated, programmable, and capable of motion on three or more axes (*3*, *4*). Self-assembly is also a powerful technique for equilibrium systems where the thermodynamic or nonequilibrium pathways are preprogrammed into the individual components or the processing techniques (*5*–*8*) but at present is limited in the complexity of the devices produced. Artificial nanoscale industrial robots add a new dimension to our nano-micro fabrication toolbox and technologies (*9*).

DNA carries genetic information through its double-stranded duplexes, established by the Watson-Crick base pairing rules. Extending this paradigm outside of the realm of genetics, the field of DNA nanotechnology seeks to use the programmability of DNA base pairing to encode structural and functional information into a designed construct at the molecular level (*10*). Over the past four decades, DNA nanotechnology has seen notable advances (*11*). Established protocols, such as DNA origami (*12*) and DNA bricks (*13*), have facilitated the creation of intricate and sophisticated structures (*12*–*22*). These advances have ushered in a new era in engineering, resulting in innovative applications ranging from machines (*20*, *21*, *23*–*29*), walkers (*30*–*34*), enzymes (*35*–*37*), self-replicators (*38*–*42*), computers (*43*–*45*), and even a one-shot nano-assembly line (*46*).

In this article, we introduce a simple DNA industrial nanorobot that can manufacture three-dimensional (3D), chiral, left- or right-handed optically active cube corners from optically inactive parts. Our nanorobot is a DNA origami cube corner with three faces (~100 nm^3) with DNA sticky end functionalized edges that can be independently programmed for selection, movement, and operation on six degrees of freedom. This robot trimer can perform the preprogrammed steps that grab three feedstock DNA origami (*17*) plates out of solution and accurately position them by stepwise folding to close the cube so that the plate edges align and bind by sticky end hybridization. Unlike a single-pot system (*47*, *48*), a user, or an external computer program, controls ultraviolet (UV) light to weld them together by UV cross-linking and changes temperature to release them into suspension. The plates are decorated with gold nanorods such that the cross-linked cube corner is chiral and optically active, unlike the unassembled plates or the robot itself. The industrial robot with its additional folding degrees of freedom also presents a solution to the problem of 3D self-replication (SR). Single-step templating in one or two dimensions requires access to the second or third dimension (*41*, *42*). Here, with folding for manipulation and positioning, our nondecorated robot cube corner can assemble a complementary cube corner robot and, in two cycles, replicate the original robot. Production then becomes exponential. Our demonstration portends nanomachines and robots programmable and controlled by light and heat for nanoscale production of nanoscale, biocompatible structures and devices.

RESULTS

Fabrication of 3D DNA industrial nanorobots

An outline for the concept, implementation, and operation of our DNA industrial robots can be found in the Discussion section of the Supplementary Materials. Our 3D fabrication process starts with the construction of the nanorobot, a cube corner–shaped DNA origami that is made by self-assembly, folding, and covalent bonding (Fig. 1A). The basic structural unit, effectively a plate, is a cross-tile DNA origami monomer made from perpendicularly organized DNA helices along the two axes (*17*), which allows us to modify the sticky ends on the edges and faces of all four cross extensions (detailed strand information can be found in fig. S3 and table S1). Further, the cross-tiles exhibit an equal (=) sign that facilitates atomic force microscopy (AFM) identification of

[1]Institute of Biomedical Engineering, Ningbo Institute of Materials Technology and Engineering, Chinese Academy of Sciences, Ningbo, China. [2]Ningbo Cixi Institute of Biomedical Engineering, Ningbo, China. [3]Department of Physics, New York University, New York, NY, USA. [4]Department of Chemistry, New York University, New York, NY, USA. [5]Department of Chemistry, Biochemistry, and Physics, Fairleigh Dickinson University, Madison, NJ, USA.
*Corresponding author. Email: zhoufeng@nimte.ac.cn (F.Z.); rs17@nyu.edu (R.S.); chaikin@nyu.edu (P.M.C.)

their orientation. The robot was made by hybridizing the complementary sticky ends on the origami monomer plates to form a 2D trimer and subsequently folding the semiflexible hinged plates 90° to fabricate a three-face cube corner using two pairs of strut strands—a short double-stranded DNA—on the adjacent planes. The length of the strut strands was determined to be 45 base pairs according to the location of the sticky ends on the origami plate, the length of the sticky ends between the origamis, and the angle between the two origami plates (Fig. 1C). We further welded the plates to stabilize the 3D structure by the cycloaddition reaction between four pairs of photo–cross-linkable 3-cyanovinylcarazole (^{CNV}K) (*49*), a pseudobase, through UV illumination (Fig. 1B). ^{CNV}K and UV for welding formed covalent bonds that were free from detachment throughout the temperature-change process, providing an additional light-controllable degree of freedom. A native gel showed that the folded-welded corner-shaped 3D trimer has a higher mobility than the 2D trimer without folding strut strands, possibly due to the smaller cross-sectional area of the 3D objects, potentially giving evidence for the formation of the 3D structure in the robot (Fig. 1D). AFM images of the robots present a closed-looped trimer structure with the designed equal sign orientation, confirming the successful cross-linking and formation of the 3D robot (Fig. 1E and fig. S4). The DNA trimer robot was stained with uranyl acetate to keep the structure intact while strongly attracted/flattened to the mica surface (*50*). The robot trimer would break apart without staining (fig. S5A).

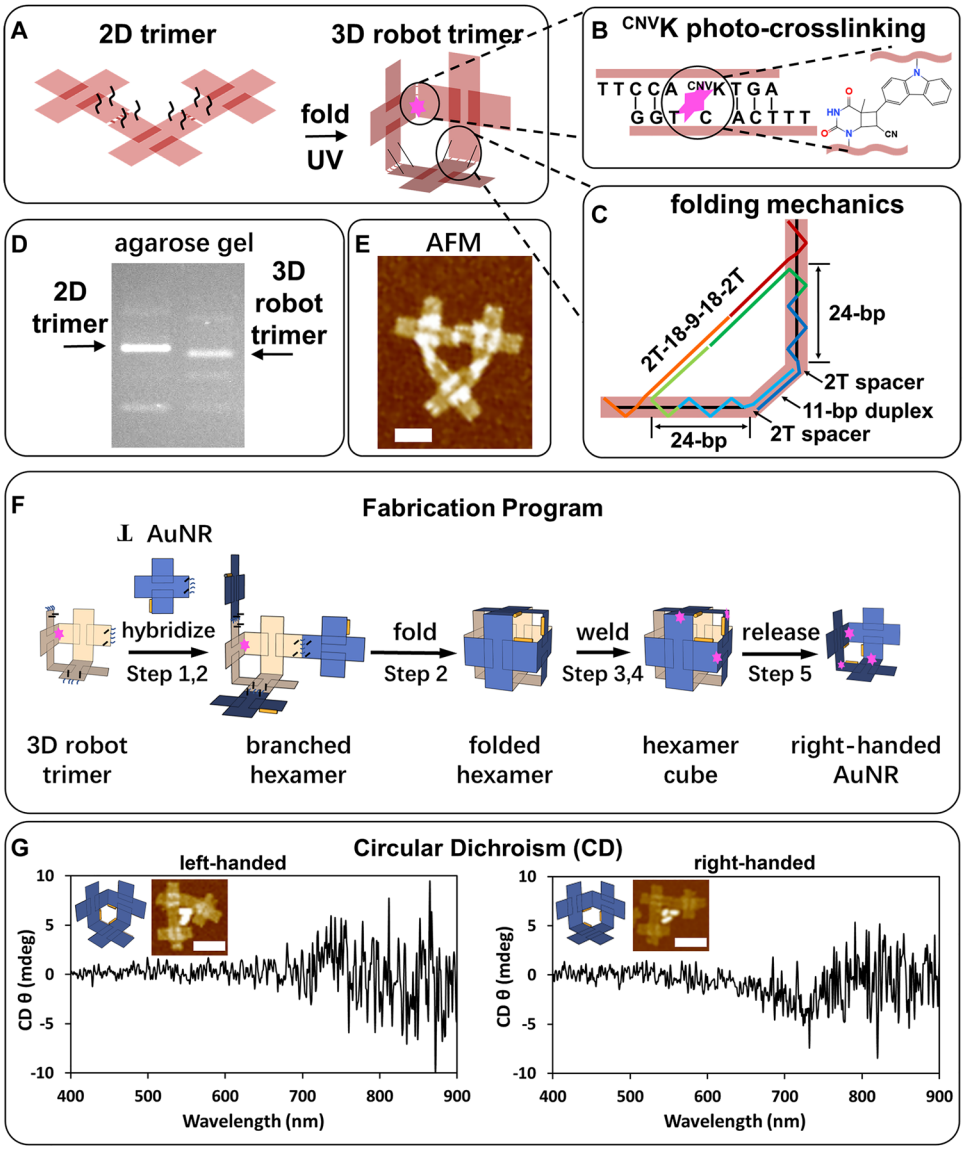

Fig. 1. Fabrication, processing, and chiral production. Schematics of (**A**) formation of 3D trimer robots by folding and UV cross-linking (purple star) of 2D trimers through (**B**) photo–cross-linking with ^{CNV}K cycloaddition reaction in the DNA duplex and (**C**) folding DNA origamis to 90° by two double-stranded DNA struts. (**D**) A nondenaturing agarose gel showing the mobility difference between the 3D robot trimer and 2D trimer. The gel was run at 48°C. (**E**) AFM of the 3D seed trimer robot. Scale bar, 50 nm. (**F**) Flowchart of the fabrication program for chiral optically active trimer constructs from achiral AuNR monomer plates and pictured preprogramming external control steps and purposes. ⊥ AuNR refers to tiles that have gold nanorods attached perpendicular to the equal sign of the cross-tile origami. (**G**) Circular dichroism spectra showing different chirality obtained by rearranging the AuNR decoration on the plates or by using a differently programmed robot. Scale bars, 100 nm.

Production of chiral nanodevices using 3D DNA industrial nanorobots

Our first demonstration, Fig. 1F, of the assembly of chiral optically active trimer constructs proceeded by introduction of the robots into a suspension of decorated monomer plates and cross-tile origami that have been decorated with a 25-nm Au nanorod (AuNR) on one cross extension. The temperature was lowered so that the plates assembled epitaxially on the edges of robot cube corners. Using their strut strands, the programmed robot arms were designed to fold the AuNR-decorated plates 90° inward to form a cubic box. The lowest temperature was set such that plates could not hybridize at their concentration in suspension. However, when they were assembled by the robot and folded to the right position, a closed cubic box, the sticky ends containing four ^{CNV}K strands on the plate edges were held in proximity, their local concentration was increased by ~10^6 (*51*), and they could hybridize. The sample was illuminated with UV light (365 nm) so that the ^{CNV}K strands could be covalently bound. The three plates together could then form a trimer cube corner with the AuNRs surrounding the vertex in a right-handed manner (fig. S6D). On heating, the product trimers could be released from the robot (fig. S6E).

The undecorated 3D robot and its products should be essentially plasmonic achiral but became plasmonic chiroptical after modification with AuNRs. All of the parts that we used were made of DNA, which should be chiral, but interactions

with red light were sufficiently weak that no circular dichroism could be observed in our apparatus. The decoration with AuNRs greatly increased the interaction with light (*52*, *53*), and the fabricated nanorod-decorated cube corners showed their difference in handedness in their circular dichroism, with inverted peaks at 720 and 800 nm (Fig. 1G). The individual plates, although they were nanorod decorated, were flat enough that the mirror plane through the flat plate rendered the system achiral (fig. S7B).

Proof of programmable fabrication and production process

To validate the fabrication process from the original robots to robot-feedstock cubic boxes and to the finished product trimers, a nondenaturing gel was conducted to study intermediate structures without AuNRs (Fig. 2). We prepared the robot face plates with and without robot–feedstock plate (FP) recognition strands and the FPs with and without folding strut strands. By design of the experiments (details in the Supplementary Materials), we could prepare the assembled structure from monomer plates to hexamer cube, folded and not folded. Lanes 7 to 10 (Fig. 2) represent the intermediate structures in the first cycle of fabrication from cube corner robot to robot-feedstock cubic box. After mixing the initial robot trimer with the excess monomer plates (no folding strut strands) and annealing from 48° to 25°C, the all-trimer band moved up to the open-branch hexamer band from lane 7 to lane 8, indicating the self-assembly of three FPs to three edges of the cube corner robot. When the folding strut strands were present, the open-branch hexamer band moved down to the closed-cube hexamer band from lane 8 to lane 9, exhibiting a similar mobility change due to the reduced cross-sectional area as those from the 2D to the 3D trimer (Fig. 1C) and from the flat dimer (lane 15) to the folded dimers (lanes 2 and 14). The hexamer band barely shifted between lane 9 and lane 10, indicating that the UV–cross-linked hexamer remained the same cubic box. In addition, we compared the open-branched, unfolded nanorobot-feedstock tetramer (lane 4), pentamer (lane 5), and hexamer (lane 8) with the folded tetramer (lane 12), pentamer (lane 11), and hexamer (lane 9). The stepwise change in the mobility (lanes 4, 5, and 8) indicates that the shape was changed over the assembly of more FPs on the DNA nanorobots. However, the mobility of the corresponding folded structures (lanes 9, 11, and 12) showed a much smaller difference compared with the unfolded structure (lanes 4, 5, and 8), indicating that all three folded structures shared a cross-sectional area similar to that of the box.

3D-templated SR of DNA nanorobots

The nanorobot we used here assembles a chiral corner cube. By changing the sticky ends and the protocols for selecting, binding, folding, and welding, we could have made a number of other structures, such as a simple two-plate elbow or chair. However, the optically active chiral corner cube has the same form and can be made to have the same functionality as the original robot (except that the edge sticky ends are complementary rather than the same). Therefore, our nanorobot can replicate itself either directly or after an intermediate complementary cycle, mimicking DNA replicating via its complement. On repeated cycles of cooling, UV illumination, and heating, the number of offspring should grow exponentially with the number of cycles. 3D-templated SR is allowed by the additional degrees of freedom enabled by precise folding.

Figure 3 shows images and gel quantification of the SR. The SR was conducted by mixing the nanorobot with first-generation (FG) monomer plates at the concentration of 0.15:1.5 nM (cycle 0). FG plates have sticky ends complementary to the robot. Second-generation (SG) monomer plates have sticky ends complementary to the FG and the same as the original robot. After the first cycle of annealing and UV cross-linking (cycle 1), the same mixture, containing both the robot trimers and the product FG trimers, was run through the nondenaturing gel at 48°C, where the FG trimers or monomers were released from the seed robot under heat (Fig. 3B). Because the structures of the robot trimer and FG trimer are the same, the gel mobility is the same, and there is only one trimer band after SR. We used the increase of trimer% from the intensity (*I*) measurement by gel electrophoresis to quantify the production and SR of the robot cube corner trimer (the detailed gel quantification

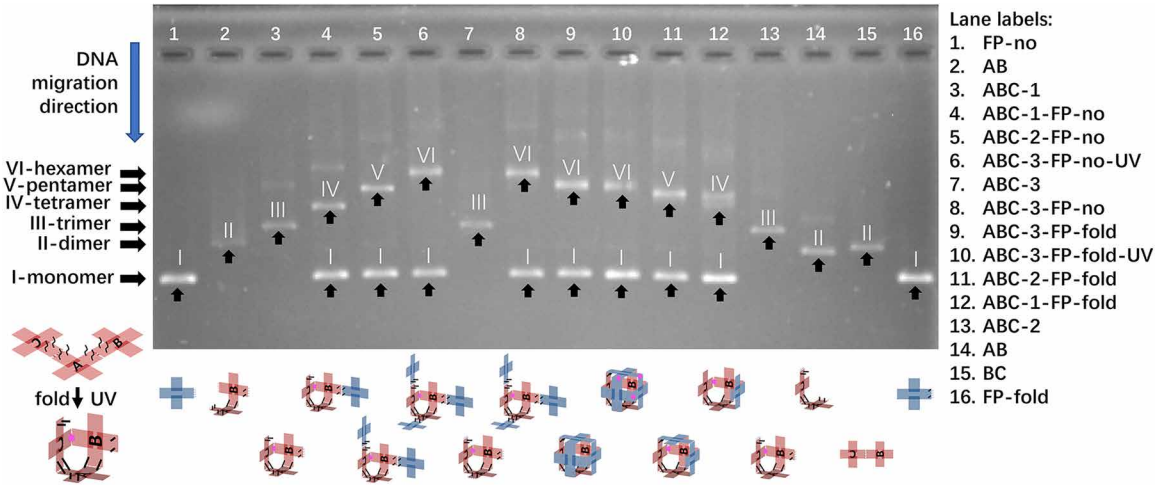

Fig.2. Intermediate structures during robot fabrication and production. The 0.8% nondenaturing agarose gel was run at 25°C at 80 V for 4 hours. We synthesized the DNA origami with different sets of sticky ends to fabricate all the intermediates in the nanorobot fabrication process (for design details, see Supplementary Discussion). The ratio between the ABC trimer robot and monomer FPs is 1:6. The example lane label "10. ABC-3-FP-fold-UV" stands for #10 lane—trimer seed made from A, B, C origami tile (each contains folding strut strands), three sets of sticky ends to assemble three FPs containing folding strut strands (UV cross-linked).

process of Fig. 3B is shown in fig. S8). The cube corner trimers increased from 13.4 to 19.4%, giving an SR rate of 1.45, with 0.45 offspring per parent. Meanwhile, no trimer was detected in the control experiment where only the FG monomer was run at the same annealing–UV illumination condition (Fig. 3B, lane control).

The trimer% was calculated using Eq. 1

$$\text{trimer}\,\% = 100 * \frac{I_{\text{trimer}}}{I_{\text{monomer}} + I_{\text{dimer}} + I_{\text{trimer}}} \quad (1)$$

The replication rate was calculated using Eq. 2

$$\text{replication rate} = \frac{\text{trimer}\,\%\,(\text{cyc1})}{\text{trimer}\,\%\,(\text{cyc0})} \quad (2)$$

The offspring per parent was calculated using Eq. 3

$$\text{offspring per parent} = \frac{\text{trimer}\,\%\,(\text{cyc1}) - \text{trimer}\,\%\,(\text{cyc0})}{\text{trimer}\,\%\,(\text{cyc0})} \quad (3)$$

The FG trimer is assembled by the robot, not self-assembled on its own. When lowering the UV cross-linking temperature to 4°C, the complementary ^{CNV}K strands on the FG monomers could hybridize and be cross-linked to form flat FG trimer structures without the presence of the robot (fig. S9). These flat trimers had different mobility than the cube corner trimer. The robot assembly showed an increase of the same trimer band with no observable addition of a flat trimer band. The robot produced its programmed structure, whereas the non-robot–templated trimer was below the detection limit using gel quantification (Fig. 3B). After release, the structure of both the robot and FG trimer product could be found on the AFM image (Fig. 3A and fig. S10), distinguished by the different equal sign orientation, verifying the production process. We identified 68 robot trimers with a parallel equal sign and 28 product trimers with a perpendicular equal sign (fig. S10), giving the comparable SR rate of 1.41 with 0.41 offspring per parent.

For successful fabrication and SR, the three face plates of the cube corner need to be placed at the right position so that the complementary ^{CNV}K strands are close enough and at a high local concentration for hybridization. Positioning accuracy is very important for successful UV cross-linking. For example, in comparison between lane 6 and lanes 8 and 10 in Fig. 2, the off-site, unfolded FG plates attached to the robot (lane 8) were difficult to UV cross-link to form the cubic box (lane 10) and on release to form the FG cube corner. When compared between lanes 6 and 8, the hexamer band was unchanged after UV illumination, indicating that the folding is essential in the UV cross-linking of the correct products. To further validate the importance of folding and positioning accuracy, we tried the replication with designed structural errors and evaluated the one-cycle SR rate. We reduced the positioning accuracy from the perfect cube design (Fig. 1F) to the "no plate folding" (Fig. 3C, i), "floppy robot" (Fig. 3C, ii), "flat robot" (Fig. 3C, iii), and "wrong-folded robot" (Fig. 3C, iv). When the cube corner robot was still intact, the absence

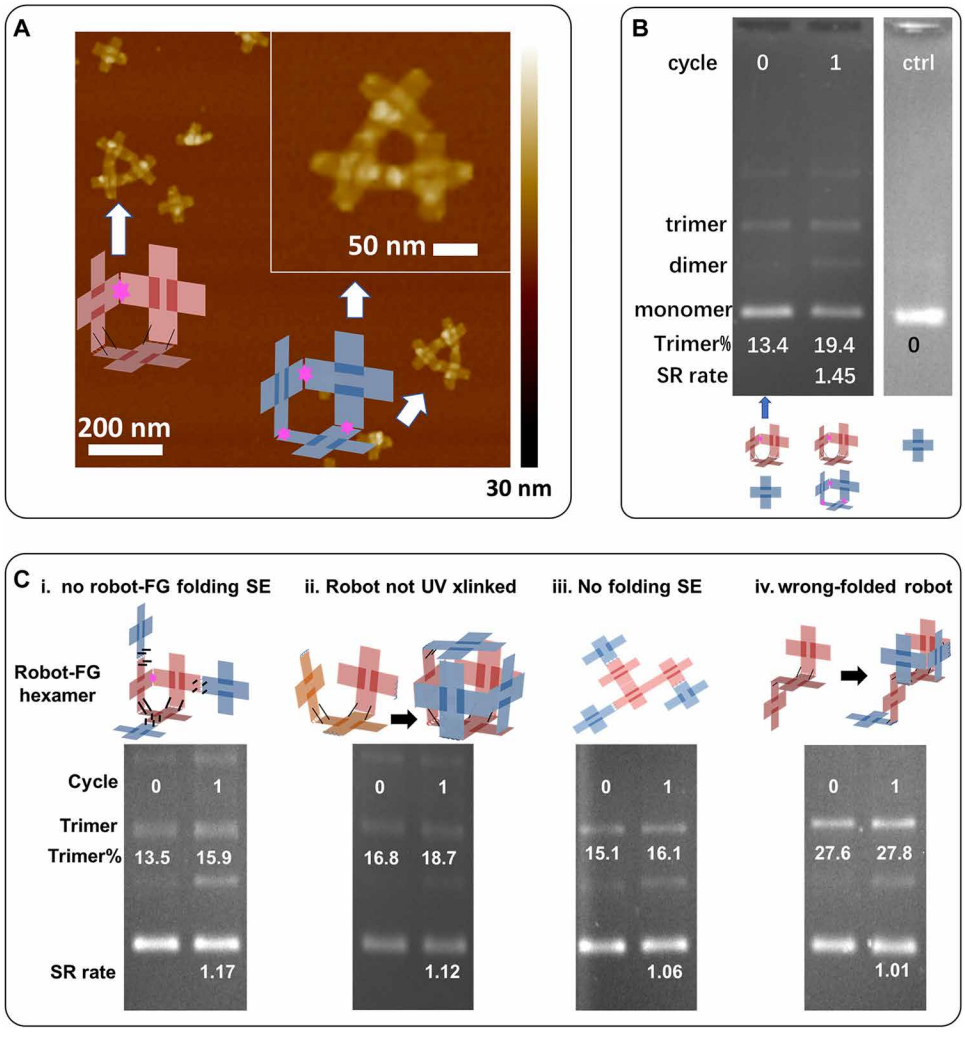

Fig.3. Analysis of robot-controlled production. (**A**) After one cycle of production, AFM shows the trimer structures with the different orientations of equal sign, enabling us to distinguish between original trimer robots (|| || or = =) and product trimer robots (all || =). The DNA trimer was stained with uranyl acetate to show the intact structure while attracted/flattened to the mica surface. (**B**) A nondenaturing agarose gel shows the SR and quantification of trimer robots after replication, with a starting ratio of 1:10 between original robot and monomer plates. Lane control (ctrl) contains the monomer plates after one cycle of the replication process. Any trimers formed without the robot were below the detection limit. (**C**) Accurate positioning is important. Misfolded robots reduce assembly efficiency. (i) No folding strands between robot and monomer plate; (ii) no UV cross-linking when making 3D robots; (iii) no folding strands on robot or monomer plate; and (iv) seed robot was folded to the wrong direction. Schematics and corresponding nondenaturing agarose gel images showing the amplification and quantification of trimers after fabrication, with a starting ratio of 1:10 between original robot and monomer plate. The robot-assisted fabrication was suppressed with an increase of error in the positioning accuracy.

of FG-robot folding sticky ends reduced the replication rate by 62.2%, from 1.45 with 0.45 offspring per parent (Fig. 3B) to 1.17 with 0.17 offspring per parent (Fig. 3C, i). Without the folding sticky ends, the FG monomers could fold freely, inward and outward, along the FG-robot hinge that contained two thymine single bases in each of the sticky ends (Fig. 1F). Then, the local concentration of the complementary ^{CNV}K strands on the assembled FG plates was smaller, as was the chance for them to be cross-linked over the UV illumination period, resulting in a smaller replication rate. When the robot was not rigidly cross-linked, the robot center was loose and wobbly, leading to the less successful FG UV cross-linking and a smaller SR rate of 1.12 with 0.12 offspring per parent (Fig. 3C, ii). With more structural errors added to the robot design, we got a much lower SR rate, 1.06 with 0.06 offspring per parent, on the non-folded flat hexamer structure (Fig. 3C, iii) and almost no production using the wrong-folded robot (Fig. 3C, iv). Although there were two FG monomers in the right position on the wrong folded robot, it was still not possible to form the FG trimer structure by UV cross-linking with the free-diffusing FG monomer in the suspension. Thus, the positioning accuracy of all the components of the FG-robot structure is essential in the fabrication of the designed cube corner product.

Multi-cycle 3D SR

After successful one-cycle 3D SR, multi-cycle SR was conducted by replenishing the UV-illuminated mixture with fresh FG and SG monomers in the subsequent cycles (Fig. 4A). Four cycles of SR experiments were conducted with the starting mixture of initial robots and FG monomer plates at a concentration of 0.5:1.5 nM. After UV illumination, a 15-μl mixture was replenished with 15 μl of 1.5:1.5 nM fresh FG:SG stock solutions. After two SR cycles, the generation of FG and SG cube corner trimers was confirmed by AFM using equal sign orientations and gold nanoparticle (AuNP) markers (figs. S11 to S14). Both FG and SG trimers had perpendicular equal sign orientations, but FG plates were modified with gold-anchoring sticky end strands that could attach 5-nm AuNPs after SR. The overall trimer percentage was decreased because of the larger monomer dilution factor compared with the trimer SR rate (Fig. 4B and fig. S15A). However, the trimer percentage kept increasing for each cycle, with a similar replication rate from 1.3 to 1.39 with 0.3 to 0.39 offspring per parent, through four cycles (Fig. 4C and fig. S15B), indicating the exponential growth of the cube corner trimer structure. A higher replication rate of 1.80 ± 0.01 ($n = 2$) with 0.80 offspring per parent could be obtained when the monomer (FG + SG)–to–seed robot trimer ratio was higher (3.375:0.075 nM), possibly because of better hexamer assembly (fig. S21A).

DISCUSSION

For most of the experiments presented here, we acted as the programming element for our robots, writing down a set of instructions and manually following the predefined program. The program consisted of turning on the temperature sweep of the automated incubator, and when the temperature reached certain predetermined values, we turned the UV light on or off. At no time did we make any measurements or observations of the sample or make corrections in the preset program. To avoid human intervention, we set up an electronic device, an Adafruit feather cortex M0 microcontroller, which turned on the UV light at a preset temperature and turned it off at a different preset temperature. We then introduced a sample of nanorobots and monomers into the incubator, switched on the incubator and electronic device, waited for the cycle to end, and removed the sample for analysis. The results are shown in fig. S22, where the replication yield was 0.47 offspring per parent.

We noted that the degradation in replication rate was higher for these trimer robots (fig. S21B) than for the dimers we have used more often (*41*). The production of trimer with robot and FG monomer mirrored this declining rate in the absence of monomer replenishment (fig. S19B). This phenomenon may well be a consequence of the stronger binding of the daughters to the parents (because there are three bonds on hybridizing rather than the single bonds joining a parent trimer to each individual monomer, and moreover, they are in the correct complementary configuration) and hence a more severe consequence of product inhibition. Our hypothesis is that this phenomenon is caused by cooperative interactions between multiple sets of binding units. Although it enables self-assembly at higher temperatures compared with individual sticky ends, it also leads to product inhibition because parent multimers have a tendency to bond with daughter multimers instead of individual monomers.

In this work, we have found an opportunity for process control based on the concentration-dependent nature of product yield or replication growth. We can compensate for the advantage of robot-to-product binding rather than robot-to-monomer binding by adding more monomers depending on the product inhibition and its enhancement to cooperative binding.

Our simple nanorobot is a step toward a manufacturing/assembly robot and can be readily extended to more complex tasks by adding more arms, folding struts, and welders. Here, we used only temperature as an actuator and ^{CNV}K and UV for welding. DNA hybridization/dehybridization can be controlled optically with different wavelengths by incorporation of photoisomers, like azobenzenes (*54*), and there are several ways of photo–cross-linking, such as cinnamate (*55*) and psoralen (*56*). Therefore, 3D DNA industrial nanorobots can be made with many controllable degrees of freedom. Because there are many polymers, plastics, metals, and other materials that can be functionalized with DNA, more diverse robots and their products can be fabricated with different compositions. DNA structures and devices are biocompatible and similar in size to organelles. These industrial nanorobots may find biomedical applications as artificial enzymes or organelles.

MATERIALS AND METHODS

Gold, DNA, and purification

Five-nanometer AuNPs in cetyltrimethylammonium bromide were purchased from Ted Pella Inc. Twenty-nanometer (20 nm by 5 nm by 5 nm) and 25-nm (25 nm by 5 nm by 5 nm) AuNRs in sodium dodecyl sulfate was purchased from Nanopartz Inc. Long single-stranded scaffold DNA m13mp18 was purchased from Bayou Biolabs. UV cross-linkable ^{CNV}K phosphoramidite was purchased from Glen Research. The single-stranded DNA sticky ends containing ^{CNV}K were synthesized on an Applied Biosystems 394 DNA synthesizer. The remaining DNA strands were purchased from Integrated DNA Technology (IDT) Inc. The sticky end strands were purified using denaturing polyacrylamide gel electrophoresis. The staple strands with thiol group were purified by IDT using high-performance liquid chromatography.

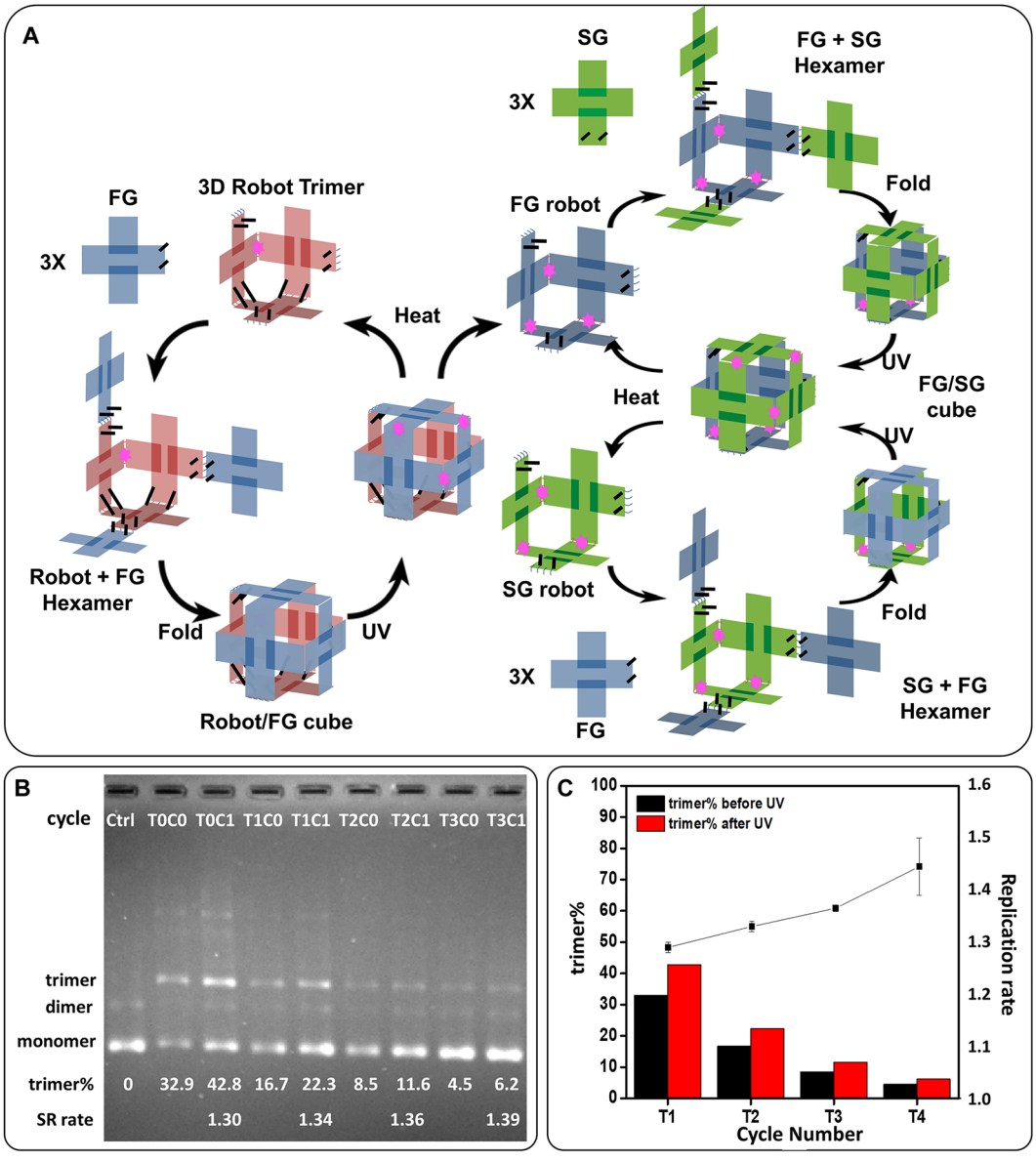

Fig.4. Robot-controlled 3D SR. (**A**) Schematic of SR cycles. With the addition of the SG monomer plates, the fabricated FG trimer robots can then act as robot templates to generate further generations. The sticky ends and folding strands are the same on the seed robot (pink) and SG monomer plate (green). The complementary sticky ends and folding strands are on the FG monomer plate (blue). (**B**) A gel image of four-cycle SR of 3D DNA trimer robots using a serial transfer. T_0C_0 in the image represents transfer 0 cycle 0. Explanation of terminology can be found in Materials and Methods. The gels were run at 48°C. (**C**) Plot showing the change of the trimer robot percentage and replication rate of each cycle of 3D trimer robot SR.

Formation of DNA origami tile monomer

Scaffold strands m13mp18 were mixed with the staple strands at a molar ratio of 1:8 in 1× TAE/Mg^{2+} buffer [40 mM tris-HCl, 20 mM acetic acid, 2.5 mM EDTA, and 12.5 mM magnesium acetate (pH 8.0)]. The final concentration of the scaffold strands was 10 nM. The mixture was placed in a thermocycling incubator through the following ramping procedure.

In the first step, the incubator was heated to 70°C at a rate of 99°C/hour and held for 20 min. In the second step, the incubator was cooled to 20°C at a rate of 7°C/hour. In the third step, the incubator was cooled to 4°C at a rate of 99°C/hour if the experiment was conducted overnight. The products were purified in 100-MW Millipore Amicon Ultra 0.5-ml centrifugal filter using 1× TAE/Mg^{2+} buffer (10 mM magnesium acetate) five times for the buffer exchange and the removal of excess staple strands.

Gold nanostructure functionalization and attachment on DNA origami

To coat the AuNPs and AuNRs with DNA, the AuNPs and AuNRs were centrifuged, and the supernatant was discarded to remove the ligands in the solution. The AuNPs and AuNRs were stabilized by buffer exchange with the fresh 2.5 mM bis(*p*-sulfonatophenyl) phenylphosphine solution five times. Thirty-two microliters of 50 μM thiolated DNA and 3 μl of 500 mM tris(2-carboxyethyl) phosphine

(TCEP) were mixed well and incubated for 1 hour. The mixture was filtered using a G25 column at 1000*g* relative centrifugal force (rcf) for 1 min to remove TCEP. The AuNP and AuNR solutions were mixed with the reduced thiolated DNA at a ratio of 1:100 for AuNPs and 1:500 for AuNRs in 0.5× tris-borate-EDTA buffer. The mixture was shaken at room temperature for 1 day. NaCl solution (5 M) was added to the mixture to increase the NaCl concentration by 25 mM at each step, and the mixture was shaken at room temperature in between. We repeated this step several times until the final concentration of NaCl was 0.2 M. The mixture was shaken overnight at 30°C and washed with 1× TAE buffer using 100,000-MW filters at 6000 rpm five times to remove the excess thiolated DNA. The DNA-coated AuNPs and AuNRs were stored in 1× TAE buffer at 4°C.

AuNPs and AuNRs were mixed with the DNA origami with the complementary gold attachment sticky ends (see fig. S3) at a ratio of 1:5. The mixture was annealed from 48°C (AuNP) or 40°C (AuNR) to room temperature at a rate of 0.7°C/hour. AFM images (fig. S6, A and B) showed that the formation of origami-AuNR monomer was above 95%. The excess AuNRs were removed by running 0.8% nondenaturing gel at 40°C. The DNA-AuNRs were recovered by gel cutting and electrophoresis elution (80 V, 40°C, 0.5-hour forward and 3-min reverse electrophoresis in a 3500-MW dialysis bag).

Formation of DNA nanorobot, the seed robot trimer

As shown in Fig. 1A, robot-A, robot-B, and robot-C monomers were preheated to 53°C for 30 min and then mixed at a concentration of 3:3:3 nM. The mixture was cooled to 16°C at a rate of 0.7°C/hour. After confirming the formation of the trimer structure with AFM and gel electrophoresis, the seed robot trimer was diluted to 0.4 nM and UV–cross-linked using the 365-nm UV light-emitting diode (LED) light (M365LP1[c], Thorlabs Inc.; power intensity, 24 mW/mm^2) at 16°C for 20 min. If prepared at high concentration, hexamer product from inter-trimer hybridization or cross-linking could happen (fig. S17).

The plasmonic chiroptical robot trimer was made by self-assembly and UV cross-linking of 20-nm AuNR-modified robot monomers (figs. S6C and S7C). The robot trimer with one AuNP marker was made by self-assembly and UV cross-linking AuNP-modified robot monomer A and non-AuNP–modified robot monomers B and C.

Production and SR cycling

The standard production and SR were conducted as follows: In the first step, the incubator was heated at 48°C for 30 min to break the robot-FG, FG-SG, and strut sticky end binding. In the second step, the incubator was cooled slowly to 16°C at a rate of 1°C/hour. In the third step, a 365-nm UV LED light was turned on for 20 min to conduct UV cross-linking inside the incubator. The environmental temperature inside the incubator was set at 16°C after screening for the lowest temperature without generating non-robot–seeded trimer (fig. S16, A and B). Seven types of production and SR were conducted using the DNA nanorobots.

Production of AuNR trimers from the undecorated DNA nanorobot

DNA nanorobot was mixed with the AuNR-modified FG monomer (FG-AuNR) at a ratio of 0.4:2 nM (Fig. 1, F and G). The control without robot trimer consisted of 2 nM FG-AuNRs. The samples were placed inside the incubator. In the first step, the incubator was heated at 40°C for 30 min to prevent AuNR detachment. In the second step, the incubator was annealed to 16°C at a rate of 1°C/hour. A robot trimer could hybridize epitaxially with three plates to form a branched hexamer. On further cooling, struts similar to those in Fig. 1C could precisely fold the plates 90° inward to form a closed cube. In the third step, a 365-nm UV LED light was turned on when the environmental temperature inside the incubator reached 16°C. The three plates in the cube were chemically cross-linked via a ^{CNV}K cycloaddition reaction. In step 4, the UV LED light was turned off after 20 min of illumination. In step 5, the sample was mixed with formaldehyde to a final concentration of 30% and heated at 30°C for 30 min to release robot trimers and product AuNR trimers.

One-cycle SR using the DNA nanorobot and FG monomer

DNA nanorobot was mixed with the FG monomer at a ratio of 0.15:1.5 nM followed by the standard 3D SR procedure (Fig. 3, A and B, and fig. S10).

Non-robot–templated control experiment using the FG-AuNP and SG–non-AuNP monomer

FG and SG monomers were mixed at a ratio of 1.8:1.8 nM followed by the standard 3D SR procedure (fig. S16C).

Multi-cycle SR using a serial transfer of fresh FG and SG monomers

Forty microliters of a solution containing 0.5 nM DNA nanorobots and 1.5 nM FG monomers was prepared (Fig. 4, B and C). A 10-μl sample was taken out to quantify the initial trimer nanorobot amount, and the rest of the solution was covered by 50 μl of silicone oil (HR3-415, HAMPTON RESEARCH) to prevent the evaporation-induced concentration change. After each cycle of standard 3D SR, a 10-μl sample was extracted for AFM imaging and nondenaturing gel electrophoresis. An additional 20 μl of fresh 1.5 nM FG and 1.5 nM SG stock solution was transferred to the original tube before the next cycle of 3D SR.

In Fig. 4B, T_0C_0 represents transfer 0 cycle 0, the sample of seed robot trimer and monomer after mixing. T_0C_1 represents transfer 0 cycle 1, the same sample after one cycle of replication. T_1C_0 represents transfer 1 cycle 0, the sample after transfer and replenishment with fresh monomers. T_1C_1 represents transfer 1 cycle 1, the sample after transfer and another cycle of SR.

Two-cycle SR with step-wise addition of FG-1AuNP and SG-0AuNP monomer plates

As shown in fig. S12, seed-robot-trimer-1Au was mixed with FG-monomer-1Au at a concentration of 0.15:1.5 nM to produce FG-trimer-3Au through the first standard SR cycle (figs. S11 to S14). Then, 8 μl of mixture was added to 16 μl of solution of 1.5 nM SG-no Au plates and went through the second standard SR cycle.

Multi-cycle experiments of trimer production with seed robot trimer and FG monomer only

Seed robot trimer and FG monomer were mixed at a ratio of 0.2:5 nM, followed by four cycles of standard 3D SR procedure (figs. S19 to S21). After three cycles of standard procedures, 30 μl of T0C3 sample was mixed with 60 μl of 5 nM FG feedstock solution to make T_1C_0, followed by four cycles of standard 3D SR procedure (fig. S20).

Multi-cycle SR experiments without replenishment

DNA nanorobot was mixed with the FG and SG monomer at a ratio of 0.075:1.8:1.575 nM, followed by four cycles of standard 3D SR procedure (fig. S21).

No-human-intervention robot-templated production procedure

DNA nanorobot was mixed with the FG and SG monomer at a ratio of 0.15:3.6:3.15 nM, followed by one cycle of standard 3D SR procedure

using an Adafruit feather cortex M0 microcontroller to control the UV light switch (fig. S22).

Nondenaturing agarose gel electrophoresis

An agarose gel (0.8%) was prepared and immersed in 1× TAE/Mg^{2+} buffer inside the gel electrophoresis box. Five-microliter samples were mixed with 1 μl of nondenaturing tracking dye (1× TAE/Mg^{2+} buffer, 50% glycerol, and trace amounts of bromophenol blue and xylene cyanol FF). The gel was run at 4 to 5 V/cm at 48°C for 3 hours. The gel was immersed in ethidium bromide (EB) solution for staining and rinsed with water to remove excess stain. The fluorescent gel image was processed using ImageJ to quantify the amount of trimers, dimers, and monomers to calculate the trimer percentage (trimer%). The growth or replication rate of each SR cycle was calculated by dividing the trimer% after UV cross-linking over the trimer% before UV crosslinking (Fig. 4B and fig. S15A). When there was no monomer replenishment (Fig. 3, B and C, and figs. S8 and S21), the trimer% before and after UV was marked as cycle 0 and cycle 1, and the SR rate was calculated as trimer% (cyc1)/trimer% (cyc0).

Gel electrophoresis purification was conducted after running the nondenaturing gel. We ran multiple lanes of the sample mixture. We cut out one lane and placed it in EB solution for staining. After rinsing and UV illumination to visualize the band position, we cut out the gel containing the target band and placed it in the dialysis bag (M_W = 3500). A second gel electrophoresis was conducted under the previous condition for 0.5 hours. The eluted solution was collected and concentrated using 100-M_W Millipore Amicon Ultra 0.5-ml centrifugal filter at a speed of 300 rcf for 1 hour. The recovering yield was 27% for the AuNR monomer plates and 14% for the robot trimer (fig. S18).

AFM imaging

AFM imaging was performed on the Nanoscope V Multimode 8 scanning probe microscope (PeakForce QNM Software, ScanAsyst-HR accessory). Silicon nitride tips (ScanAsyst-Air; Bruker Nano Inc.) were used for peakforce mode in air. Silicon nitride tips (ScanAsyst-liquid; Bruker Nano Inc.) were used for peakforce mode in liquid.

For seed robot trimer formation (Fig. 1E and fig. S4), 2 μl of diluted sample was mixed with 4 μl of 1% uranyl acetate in 1× TAE/Mg^{2+} solution for 1 min and deposited on a clean mica surface (Ted Pella Inc.) for 1 min. The mica was then washed with 50 to 70 μl of double-distilled water three times and subsequently dried using N_2.

For SR results (Fig. 3A), the DNA trimer was stained with uranyl acetate to show the intact structure while sitting on the mica surface. The fresh-cleaved mica substrate, 2 μl of diluted sample, and 4 μl of 1% uranyl acetate in 1× TAE/Mg^{2+} solution were heated at 48°C for 30 min. Then, after the same mixing, the deposition and washing step as demonstrated above was executed to prepare AFM in the air sample.

For SR results marked by AuNRs (Fig. 1G and figs. S6 and S7C) or AuNPs (figs. S11 to S14 and S16C), the heat release at 48°C could detach the DNA sticky ends on the gold surface and remove the gold marker from the DNA origami. To lower the dehybridization temperature for heat release, the samples were mixed with formaldehyde to 30%, and the AFM samples were prepared at 30°C.

Circular dichroism

Circular dichroism was conducted on a Jasco J-1500 circular dichroism spectrometer with the standard UV-visible detector. A 100-μl sample was placed in the cuvette with a window width of 2 mm and a depth of 10 mm. The sample spectra were corrected by subtraction with the blank measurement of 1× TAE/Mg^{2+} buffer.

Statistical methods

Mean and error bars to represent the SDs were used for statistical analysis in quantifying the growth and SR rate using Origin 2022 (OriginLab Corp.) We used the gel results to quantify the growth and to compare the SR rate and regarded the wide-scan AFM data (figs. S10, S13, S14, and S16C) as semiquantitative corroboration. The statistical data (Fig. 4C) were calculated on the basis of gel electrophoresis results in Fig. 4B and fig. S15A. The detailed calculation was included as fig. S15B.

Supplementary Materials

This PDF file includes:

Supplementary Discussion
Figs. S1 to S24
Table S1
References (*57*, *58*)

Other Supplementary Material for this manuscript includes the following:

MDAR Reproducibility Checklist

REFERENCES AND NOTES

1. K. Chen, F. H. Arnold, Engineering new catalytic activities in enzymes. *Nat. Catal.* **3**, 203–213 (2020).
2. J. A. Doudna, V. L. Rath, Structure and function of the eukaryotic ribosome. *Cell* **109**, 153–156 (2002).
3. V. Zykov, E. Mytilinaios, B. Adams, H. Lipson, Self-reproducing machines. *Nature* **435**, 163–164 (2005).
4. A. Abdel-Rahman, C. Cameron, B. Jenett, M. Smith, N. Gershenfeld, Self-replicating hierarchical modular robotic swarms. *Commun. Eng.* **1**, 35 (2022).
5. S. Li, R. Batra, D. Brown, H. D. Chang, N. Ranganathan, C. Hoberman, D. Rus, H. Lipson, Particle robotics based on statistical mechanics of loosely coupled components. *Nature* **567**, 361–365 (2019).
6. C. A. Mirkin, R. L. Letsinger, R. C. Mucic, J. J. Storhoff, A DNA-based method for rationally assembling nanoparticles into macroscopic materials. *Nature* **382**, 607–609 (1996).
7. W. Liu, J. Halverson, Y. Tian, A. V. Tkachenko, O. Gang, Self-organized architectures from assorted DNA-framed nanoparticles. *Nat. Chem.* **8**, 867–873 (2016).
8. A. Kuzyk, R. Schreiber, Z. Fan, G. Pardatscher, E. M. Roller, A. Högele, F. C. Simmel, A. O. Govorov, T. Liedl, DNA-based self-assembly of chiral plasmonic nanostructures with tailored optical response. *Nature* **483**, 311–314 (2012).
9. S. Kassem, A. T. Lee, D. A. Leigh, A. Markevicius, J. Solà, Pick-up, transport and release of a molecular cargo using a small-molecule robotic arm. *Nat. Chem.* **8**, 138–143 (2016).
10. N. C. Seeman, Nucleic acid junctions and lattices. *J. Theor. Biol.* **99**, 237–247 (1982).
11. N. C. Seeman, *Structural DNA Nanotechnology* (Cambridge Univ. Press, 2015).
12. P. W. Rothemund, Folding DNA to create nanoscale shapes and patterns. *Nature* **440**, 297–302 (2006).
13. Y. Ke, L. L. Ong, W. M. Shih, P. Yin, Three-dimensional structures self-assembled from DNA bricks. *Science* **338**, 1177–1183 (2012).
14. S. W. Schaffter, J. Schneider, D. K. Agrawal, M. S. Pacella, E. Rothchild, T. Murphy, R. Schulman, Reconfiguring DNA nanotube architectures via selective regulation of terminating structures. *ACS Nano* **14**, 13451–13462 (2020).
15. S. M. Douglas, H. Dietz, T. Liedl, B. Högberg, F. Graf, W. M. Shih, Self-assembly of DNA into nanoscale three-dimensional shapes. *Nature* **459**, 414–418 (2009).
16. E. S. Andersen, M. Dong, M. M. Nielsen, K. Jahn, R. Subramani, W. Mamdouh, M. M. Golas, B. Sander, H. Stark, C. L. P. Oliveira, J. S. Pedersen, V. Birkedal, F. Besenbacher, K. V. Gothelf, J. Kjems, Self-assembly of a nanoscale DNA box with a controllable lid. *Nature* **459**, 73–76 (2009).
17. W. Liu, H. Zhong, R. Wang, N. C. Seeman, Crystalline two-dimensional DNA-origami arrays. *Angew. Chem. Int. Ed.* **50**, 264–267 (2011).
18. N. C. Seeman, H. F. Sleiman, DNA nanotechnology. *Nat. Rev. Mater* **3**, 1–23 (2017).
19. Y. Ke, T. Meyer, W. M. Shih, G. Bellot, Regulation at a distance of biomolecular interactions using a DNA origami nanoactuator. *Nat. Commun.* **7**, 1–8 (2016).

20. T. Gerling, K. F. Wagenbauer, A. M. Neuner, H. Dietz, Dynamic DNA devices and assemblies formed by shape-complementary, non–base pairing 3D components. *Science* **347**, 1446–1452 (2015).
21. A. E. Marras, L. Zhou, H.-J. Su, C. E. Castro, Programmable motion of DNA origami mechanisms. *Proc. Natl. Acad. Sci. U.S.A.* **112**, 713–718 (2015).
22. B. Wei, M. Dai, P. Yin, Complex shapes self-assembled from single-stranded DNA tiles. *Nature* **485**, 623–626 (2012).
23. G. Zhu, M. Hannel, R. Sha, F. Zhou, M. Y. Ben Zion, Y. Zhang, K. Bishop, D. Grier, N. Seeman, P. Chaikin, Microchemomechanical devices using DNA hybridization. *Proc. Natl. Acad. Sci. U.S.A.* **118**, e2023508118 (2021).
24. B. Yurke, A. J. Turberfield, A. P. Mills, F. C. Simmel, J. L. Neumann, A DNA-fuelled molecular machine made of DNA. *Nature* **406**, 605–608 (2000).
25. R. A. Muscat, J. Bath, A. J. Turberfield, A programmable molecular robot. *Nano Lett.* **11**, 982–987 (2011).
26. E. Kopperger, J. List, S. Madhira, F. Rothfischer, D. C. Lamb, F. C. Simmel, A self-assembled nanoscale robotic arm controlled by electric fields. *Science* **359**, 296–301 (2018).
27. S. M. Douglas, I. Bachelet, G. M. Church, A logic-gated nanorobot for targeted transport of molecular payloads. *Science* **335**, 831–834 (2012).
28. M. Akter, J. J. Keya, K. Kayano, A. M. R. Kabir, D. Inoue, H. Hess, K. Sada, A. Kuzuya, H. Asanuma, A. Kakugo, Cooperative cargo transportation by a swarm of molecular machines. *Sci. Robot.* **7**, eabm0677 (2022).
29. L. Liu, A localized DNA finite-state machine with temporal resolution. *Sci., Adv.* **8**, eabm9530 (2022).
30. C. Jung, P. Allen, A. Ellington, A stochastic DNA walker that traverses a microparticle surface. *Nat. Nanotechnol.* **11**, 157–163 (2016).
31. W. B. Sherman, N. C. Seeman, A precisely controlled DNA biped walking device. *Nano Lett.* **4**, 1203–1207 (2004).
32. A. J. Thubagere, W. Li, R. F. Johnson, Z. Chen, S. Doroudi, Y. L. Lee, G. Izatt, S. Wittman, N. Srinivas, D. Woods, E. Winfree, L. Qian, A cargo-sorting DNA robot. *Science* **357, eaan6558**, (2017).
33. X. Qu, D. Zhu, G. Yao, S. Su, J. Chao, H. Liu, X. Zuo, L. Wang, J. Shi, L. Wang, W. Huang, H. Pei, C. Fan, An exonuclease III-powered, on-particle stochastic DNA walker. *Angew. Chem. Int. Ed.* **56**, 1855–1858 (2017).
34. T. Omabegho, R. Sha, N. C. Seeman, A bipedal DNA Brownian motor with coordinated legs. *Science* **324**, 67–71 (2009).
35. G. Grossi, M. D. E. Jepsen, J. Kjems, E. S. Andersen, Control of enzyme reactions by a reconfigurable DNA nanovault. *Nat. Commun.* **8**, 1–8 (2017).
36. M. Liu, J. Fu, C. Hejesen, Y. Yang, N. W. Woodbury, K. Gothelf, Y. Liu, H. Yan, A DNA tweezer-actuated enzyme nanoreactor. *Nat. Commun.* **4**, 2127 (2013).
37. S. Zhao, F. Duan, S. Liu, T. Wu, Y. Shang, R. Tian, J. Liu, Z. G. Wang, Q. Jiang, B. Ding, Efficient intracellular delivery of RNase A using DNA origami carriers. *ACS Appl. Mater. Interfaces* **11**, 11112–11118 (2019).
38. T. Wang, R. Sha, R. Dreyfus, M. E. Leunissen, C. Maass, D. J. Pine, P. M. Chaikin, N. C. Seeman, Self-replication of information-bearing nanoscale patterns. *Nature* **478**, 225–228 (2011).
39. R. Schulman, B. Yurke, E. Winfree, Robust self-replication of combinatorial information via crystal growth and scission. *Proc. Natl. Acad. Sci. U.S.A.* **109**, 6405–6410 (2012).
40. T. Li, K. Nicolaou, Chemical self-replication of palindromic duplex DNA. *Nature* **369**, 218–221 (1994).
41. X. He, R. Sha, R. Zhuo, Y. Mi, P. M. Chaikin, N. C. Seeman, Exponential growth and selection in self-replicating materials from DNA origami rafts. *Nat. Mater.* **16**, 993–997 (2017).
42. R. Zhuo, F. Zhou, X. He, R. Sha, N. C. Seeman, P. M. Chaikin, Litters of self-replicating origami cross-tiles. *Proc. Natl. Acad. Sci. U.S.A.* **116**, 1952–1957 (2019).
43. D. Woods, D. Doty, C. Myhrvold, J. Hui, F. Zhou, P. Yin, E. Winfree, Diverse and robust molecular algorithms using reprogrammable DNA self-assembly. *Nature* **567**, 366–372 (2019).
44. X. Xiong, T. Zhu, Y. Zhu, M. Cao, J. Xiao, L. Li, F. Wang, C. Fan, H. Pei, Molecular convolutional neural networks with DNA regulatory circuits. *Nat. Mach. Intell.* **4**, 625–635 (2022).
45. G. Chatterjee, N. Dalchau, R. A. Muscat, A. Phillips, G. Seelig, A spatially localized architecture for fast and modular DNA computing. *Nat. Nanotechnol.* **12**, 920–927 (2017).
46. H. Gu, J. Chao, S.-J. Xiao, N. C. Seeman, A proximity-based programmable DNA nanoscale assembly line. *Nature* **465**, 202–205 (2010).
47. N. Paul, G. F. Joyce, A self-replicating ligase ribozyme. *Proc. Natl. Acad. Sci. U.S.A.* **99**, 12733–12740 (2002).
48. G. F. Joyce, J. W. Szostak, Protocells and RNA self-replication. *Cold Spring Harb. Perspect. Biol.* **10**, (2018).
49. Y. Yoshimura, K. Fujimoto, Ultrafast reversible photo-cross-linking reaction: Toward in situ DNA manipulation. *Org. Lett.* **10**, 3227–3230 (2008).
50. F. Zhou, W. Sun, C. Zhang, J. Shen, P. Yin, H. Liu, 3D freestanding DNA nanostructure hybrid as a low-density high-strength material. *ACS Nano* **14**, 6582–6588 (2020).
51. F. Zhou, R. Sha, H. Ni, N. Seeman, P. Chaikin, Mutations in artificial self-replicating tiles: A step toward Darwinian evolution. *Proc. Natl. Acad. Sci. U.S.A.* **118**, e2111193118 (2021).
52. A. Kuzyk, R. Schreiber, H. Zhang, A. O. Govorov, T. Liedl, N. Liu, Reconfigurable 3D plasmonic metamolecules. *Nat. Mater.* **13**, 862–866 (2014).
53. L. Xin, X. Duan, N. Liu, Dimerization and oligomerization of DNA-assembled building blocks for controlled multi-motion in high-order architectures. *Nat. Commun.* **12**, 3207 (2021).
54. H. Asanuma, X. Liang, H. Nishioka, D. Matsunaga, M. Liu, M. Komiyama, Synthesis of azobenzene-tethered DNA for reversible photo-regulation of DNA functions: Hybridization and transcription. *Nat. Protoc.* **2**, 203–212 (2007).
55. L. Feng, J. Romulus, M. Li, R. Sha, J. Royer, K. T. Wu, Q. Xu, N. C. Seeman, M. Weck, P. Chaikin, Cinnamate-based DNA photolithography. *Nat. Mater.* **12**, 747–753 (2013).
56. S. T. Isaacs, C.-K. J. Shen, J. E. Hearst, H. Rapoport, Synthesis and characterization of new psoralen derivatives with superior photoreactivity with DNA and RNA. *Biochemistry* **16**, 1058–1064 (1977).
57. J. B. Mills, E. Vacano, P. J. Hagerman, Flexibility of single-stranded DNA: Use of gapped duplex helices to determine the persistence lengths of poly(dT) and poly(dA). *J. Mol. Biol.* **285**, 245–257 (1999).
58. H. Ni, X. Fan, F. Zhou, G. Guo, J. Y. Lee, N. C. Seeman, D. N. Kim, N. Yao, P. M. Chaikin, Y. Han, Direct visualization of floppy two-dimensional DNA origami using cryogenic electron microscopy. *iScience* **25**, 104373 (2022).

Acknowledgments

Funding: This work was supported by Department of Energy DE-SC0007991 (P.M.C., N.C.S., R.S., and F.Z.); Department of Energy DE-SC0020976 (P.M.C.); Center for Bio-Inspired Energy Sciences, an Energy Frontier Research Center funded by the Department of Energy, Office of Sciences, Basic Energy Sciences, DE-SC0000989 (P.M.C., H.N., G.Z., and L.B.); National Science Foundation 2106790 (R.S. and N.C.S.); Office of Naval Research N000141912596 (R.S. and N.C.S.); and Human Frontiers Science Program RGP0010/2017 (R.S. and N.C.S.). **Author contributions:** Conceptualization: P.M.C., N.C.S., R.S., and F.Z. Methodology: R.S., F.Z., H.N., G.Z., and L.B. Investigation: P.M.C., N.C.S., R.S., F.Z., H.N., G.Z., and L.B. Visualization: F.Z., H.N., G.Z., and L.B. Funding acquisition: P.M.C. and N.C.S. Project administration: P.M.C. and N.C.S. Supervision: P.M.C. and N.C.S. Writing—original draft: P.M.C., N.C.S., and F.Z. Writing—review and editing: P.M.C., N.C.S., R.S., F.Z., H.N., G.Z., and L.B. **Competing interests:** The authors declare that they have no competing interests. **Data and materials availability:** All data needed to support the conclusions of this manuscript are included in the main text or Supplementary Materials. Raw data and the code to operate the Adafruit feather cortex M0 microcontroller are available in an online repository (https://doi.org/10.5061/dryad.tdz08kq5h).

Submitted 30 September 2022
Accepted 7 November 2023
Published 6 December 2023
10.1126/scirobotics.adf1274

Science Robotics

Toward three-dimensional DNA industrial nanorobots

Feng Zhou, Heng Ni, Guolong Zhu, Lev Bershadsky, Ruojie Sha, Nadrian C. Seeman, and Paul M. Chaikin

Sci. Robot. **8** (85), eadf1274. DOI: 10.1126/scirobotics.adf1274

Science Robotics (ISSN 2470-9476) is published by the American Association for the Advancement of Science. 1200 New York Avenue NW, Washington, DC 20005. The title *Science Robotics* is a registered trademark of AAAS.